Active sites and mechanism of aqueous phase methanol dehydrogenation on Pt/Al_2O_3 catalysts from multiscale modeling, microkinetic modeling, and operando spectroscopy

Ricardo A. Garcia Carcamo,^{†,¶} Tianjun Xie,^{†,§} Bryan J. Hare,[‡] Carsten Sievers,[‡] and Rachel B. Getman*,^{†,¶}

†Department of Chemical and Biomolecular Engineering, Clemson University, Clemson, SC 29634, United States

‡School of Chemical and Biomolecular Engineering, Georgia Institute of Technology,

Atlanta, GA 30332, United States

¶Current affiliation: William G. Lowrie Department of Chemical and Biomolecular Engineering, The Ohio State University, Columbus, OH 43220

§Current affiliation: Department of Chemical, Biological and Bioengineering, North Carolina Agricultural and Technical State University, Greensboro, NC 27411

E-mail: getman.11@osu.edu

Abstract

One of the most important scientific challenges of the decade is to design catalysts that produce H_2 from "minimum CO_2 " sources. One way to do this is by aqueous phase reforming (APR) of sugar alcohol molecules derived from biomass. However, to date, H_2 yields have been disappointing, indicating a need to optimize catalysts and

reaction conditions to improve H_2 production. This requires a detailed understanding of the APR mechanism. There are three primary steps: dehydrogenation, decarbonylation, and water gas shift. However, the details of these steps remain unknown due to the large and complex structures of the reactant molecules, the aqueous reaction conditions, and the participation of multiple types of active sites in the mechanism. To begin to address these knowledge gaps, herein we study the effect of liquid H_2O solvent and multiple types of active sites on the mechanism of CH_3OH dehydrogenation. Specifically, we use a combination of multiscale modeling, microkinetic modeling, and Fourier transfor infrared spectroscopy to determine the mechanism of CH_3OH dehydrogenation on Pt/Al_2O_3 catalysts. We investigate sites on the terraces of large Pt particles as well as sites at the Pt/Al_2O_3 perimeter and the influence of liquid H_2O on both. We show that the reaction is carried out on terrace sites due to inhibition by strongly bound H_2O molecules at perimeter sites. We further show that water plays a significant role in the CH_3OH dehydrogenation mechanism on Pt terrace sites but that these changes do not influence the observed rate of CH_3OH consumption.

1 Introduction

Biomass is an important energy source for the transition to a more sustainable energy market. Among biomass products, hydrogen is an emerging alternative to fossil fuels with environmental and economic benefits. 1,2 Hydrogen derived from biomass is particularly promising for biorefining. The hydrogen that is produced can be used in other biorefinery reactions such as hydrodeoxygenation; ti can also be used in Fischer-Tropsch synthesis or to produce electricity. One way to produce H_2 (g) from biomass is through aqueous phase reforming (APR) of oxygenate species or sugars such as saccharides and polyols. APR employs metal catalysts, typically over metal oxide or carbon-based supports 8,9 and an aqueous phase environment. The APR mechanism comprises three sub-processes, i.e., dehydrogenation, decarbonylation, and water gas shift (WGS). $^{10-12}$ Typical reaction conditions are temper-

ature ~ 500 K, pressure between 10-50 bar, and feedstock concentration between 1-10%. ¹³ Some industrially relevant feedstocks are ethanol, ¹⁴ glycerol, ¹⁵ ethylene glycol, ¹⁶ sorbitol, ¹⁷ sucrose, ¹⁸ and glucose. ¹⁹ However, the broader adoption of APR technology is inhibited by low H₂ (g) yields and catalyst deactivation. ^{10,20}

A key step in the development of better catalysts is garnering a molecular-level understanding of the catalytic mechanism. In APR, this is complicated by the aqueous environment as well as the variety of catalyst active sites in the system. The aqueous environment plays multiple roles in the catalysis, such as modifying thermodynamic and kinetic quantities, ^{21,22} altering the dominant reaction pathways, ^{23–25} and participating in the mechanism, e.g., via site blocking, ²⁶ modification of the active site, ^{27,28} and mediating hydrogen transfer. ^{23,29} The variety of active sites arises from the inherent activity of metal oxide or carbon-based materials for oxygenate feedstocks ³⁰ and the sensitivity of the mechanism to the structure of the active site. ^{2,31} Indeed, Heyden and co-workers showed that the metal/support perimeter likely plays a role in WGS catalysis. ³⁷ Alumina is a widely used support because it comprises Lewis acid sites ³² that provide anchoring points for oxygenate species ^{33,34} and high propensity for hydrogen production. ^{10,13,17,35,36}

However, details about the active sites and mechanisms of the dehydrogenation and decarbonylation sub-processes remain unknown. In fact, this information is unresolved even for the simplest oxygenate, methanol. This is despite decades of research into the mechanism of methanol decomposition due to its importance to electrocatalysis, ³⁸ direct fuel cells, ³⁹ and CO₂ reduction, ⁴⁰ in addition to APR. Prior research suggests that interactions between water and the alumina support influence the chemistry. Specifically, our groups ⁴¹ showed that large metal particles are more active for aqueous phase methanol dehydrogenation than small metal particles, suggesting that the reaction is favored on the more highly coordinated metal sites, i.e., on metal terraces, than on the undercoordinated sites at the metal/support perimeter. We further showed that the presence of water inhibits activity on small metal particles but has no effect on the activity of large metal particles. However, the mechanistic

reasons for this remain unresolved. Multiple groups have shown using molecular simulations that the reaction mechanism for dehydrogenation is different on terrace sites than it is on perimeter sites in gas phase, ^{34,42,43} and our groups have shown that in aqueous phase, the strongly bound water layer destabilizes interfacial species due to a cavity effect. ⁴⁴ However, how this influences the mechanism and rate of methanol dehydrogenation remains to be resolved.

There are hence multiple outstanding knowledge gaps about the mechanism of methanol APR. Towards the goal of closing these knowledge gaps, our objective in this work is to clarify the active sites and mechanism for methanol dehydrogenation on Pt/Al_2O_3 catalysts. To do this, we use a combination of multiscale simulations, ^{34,44–46} microkinetic modeling, and Fourier transform infrared spectroscopy (FTIR). ⁴¹ We show that the active sites for CH_3OH dehydrogenation are on the terraces of large Pt particles and that sites at the Pt/Al_2O_3 perimeter are inactive. This is because strongly bound H_2O* molecules inhibit CH_3OH* molecules from binding at the Pt/Al_2O_3 perimeter. Further, these H_2O* molecules protonate CH_xO* species at the Pt/Al_2O_3 perimeter, hence pushing the reaction in reverse. These effects do not occur on Pt terrace sites, and hence, the rate is only minorly affected by the aqueous phase. Interestingly, the mechanism on terrace sites is significantly impacted by the water solvent. Specifically, liquid H_2O molecules promote significant stabilization of CH_2OH* and COH* species, which forces the mechanism through a $COH-H_2O*$ intermediate that alters the equilibrium between COH* and CO*.

2 Methodology

2.1 Models

Making comparisons between experiments and theory requires constructing models that can be used along with experimental observations to explain the observed behavior. In this work, FTIR experiments are performed on both "large" and "small" Pt particles, which have average particle sizes of 4.6 nm and 1.0 nm, respectively. Both particle sizes comprise sites on Pt terraces as well as at the Pt/Al₂O₃ perimeter (Figure 1). However, the larger Pt particles will have a greater fraction of terrace sites whereas the smaller Pt particles will have a greater fraction of perimeter sites. Hence, differences in activity between the two particle sizes, along with insights from modeling, can be used as a probe of the relative activity on terrace versus perimeter sites. Following prior work^{34,44}, we use a Pt(111) slab to model terrace sites and a Pt cluster anchored to an Al₂O₃ slab to model Pt/Al₂O₃ perimeter sites. While this choice of models is a simplification of real nanometer-sized Pt particles on Al₂O₃, it allows for studying the extent to which interactions with the support affect the reaction path of methanol on Pt.

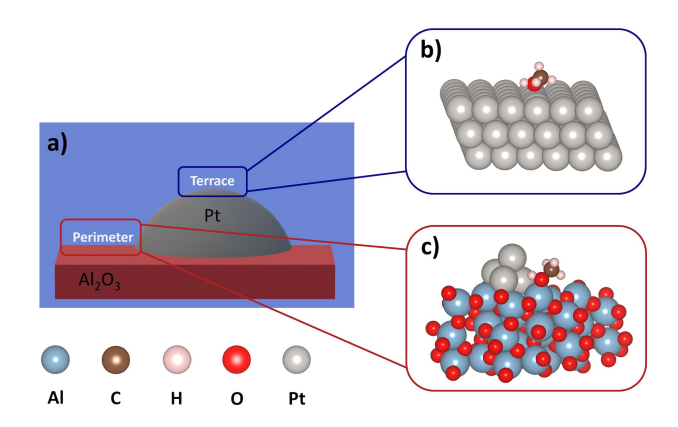


Figure 1: Pt/Al_2O_3 site models. a) Cartoon representation of a supported Pt catalyst. b) Terrace site model. c) Perimeter site model.

2.2 Microkinetic Modeling

Microkinetic modeling is carried out using the MKMCXX software. $^{47-49}$ The operation temperature is set to 500 K. The bulk phase concentration of CH_3OH is set to 10%. In gas phase models, an inert N_2 (g) gas comprises the remaining 90%, while water comprises the remaining 90% in aqueous phase models. The pressure is set to 1 bar in all models and remains constant over the simulation. In practice, APR is carried out near the vapor pressure of water at the reaction temperature, to maintain condensed phase conditions. In our mod-

eling, condensed phase conditions are maintained using multiscale modeling with explicit liquid water. ⁴⁴ Hence, the sole function of the pressure is to compute gas phase collision frequencies for adsorption/desorption reactions. How these are modeled is discussed below. Microkinetic models are run until the changes in the fractional coverages of all of the reaction intermediates between successive iterations are less than 10⁻¹² ML (10⁸ s for terrace sites and 10¹⁰ s for perimeter sites; see Supporting Information Section 1.4). The degree of rate control (DRC) is calculated using the MKMCXX software, ^{47,49} which follows the method of Campbell and coworkers. ⁵⁰

2.3 Possible Reaction Steps

The following elementary steps are considered in the microkinetic models:

$$CH_3OH + * \rightleftharpoons CH_3OH*$$
 (1)

$$H_2O + * \rightleftharpoons H_2O*$$
 (2)

$$CH_3OH* + * \rightleftharpoons CH_2OH* + H*$$
 (3)

$$CH_2OH* + * \rightleftharpoons CHOH* + H* \tag{4}$$

$$CHOH* + * \rightleftharpoons COH* + H* \tag{5}$$

$$COH* + * \rightleftharpoons CO* + H* \tag{6}$$

$$COH* + H2O \rightleftharpoons COH - H2O*$$
 (7)

$$\mathrm{COH-H_2O*} + * \rightarrow \mathrm{CO*} + \mathrm{H*} + \mathrm{H_2O} \tag{8}$$

$$CH_3OH* + * \rightleftharpoons CH_3O* + H*$$
(9)

$$CH_3O* + * \rightleftharpoons CH_2O* + H* \tag{10}$$

$$CH_2O* + * \rightleftharpoons CHO* + H* \tag{11}$$

$$CHO* + * \rightleftharpoons CO* + H* \tag{12}$$

$$CH_2OH* + * \rightleftharpoons CH_2O* + H*$$
(13)

$$CHOH* + * \rightleftharpoons CHO* + H* \tag{14}$$

$$CO* \rightleftharpoons CO + *$$
 (15)

$$H* \rightleftharpoons \frac{1}{2}H_2 + * \tag{16}$$

where "*" is an adsorption site and "*'ed" species are adsorbed to the catalyst. Structures of adsorbed species can be found in Supporting Information Section 3. Steps 1-16 are chosen based on prior work by López, ⁴³ Mavrikakis, ⁵¹ Neurock, ⁴² Asthagiri, ⁵² Janik, ⁵³ Zhou and Li, ⁵⁴ and our group. ^{34,45} Of the steps listed, those involving H₂O (e.g., rxn 2) are not included in gas phase microkinetic models. Further, H₂O adsorption is not included in the aqueous phase terrace site model because the binding energy of H₂O is significantly weaker than for CH₃OH on Pt(111). ^{55,56} Finally, H₂O-catalyzed COH* dehydrogenation (rxns 7 and 8) is not included in the aqueous phase perimeter site model, since by inspection (see Supporting Information Figure 10g) the O-H bond on COH* in perimeter sites is inaccessible to H₂O. (We additionally show below that COH* does not form on perimeter sites, so the reaction is irrelevant anyways.)

In addition to steps 1-16, we investigate reactions where H_2O* donates a proton to a partially dehydrogenated species and converts to OH*,e.g., $CH_2O* + H_2O* \rightleftharpoons CH_2OH* + OH*$ (see Supporting Information Section 1.3). We find that this type of reaction is unfavorable at terrace sites; however, some such reactions are feasible at perimeter sites. Effects of these steps on the mechanism and rate are discussed below and in Supporting Information Section 1.3.

C-O cleavage and hydrogenolysis reactions are not included in our models since they are

thermodynamically ⁵⁷ and kinetically unfavorable, ^{42,58} respectively. The Boudard reaction ⁵⁹ $(2\text{CO}* \longrightarrow \text{CO}_2* + \text{C}*)$ is not included since activity is suppressed below 673 K ⁶⁰ (while APR is carried out ~500 K). Finally, any step 1-16 with calculated free energy (see Table 1) more positive than 0.30 eV is not included in microkinetic modeling.

2.4 Rate Constants

Rate constants for surface reactions are calculated using the equations:

$$k_{\text{fw}} = A_{\text{fw}} \exp\left(\frac{-\Delta F_{\text{act,fw}}}{k_B \cdot T}\right)$$
 (17)

$$k_{\rm bw} = k_{\rm fw}/K_{\rm eq} \tag{18}$$

$$K_{\rm eq} = \exp\left(\frac{-\Delta F_{\rm rxn}}{k_B \cdot T}\right) \tag{19}$$

where "fw" denotes the forward reaction, "bw" denotes the backward reaction, A is the pre-exponential term, F is the calculated free energy, k_B is Boltzmann's constant, and T is the reaction temperature. $A_{\rm fw}$ and $A_{\rm bw}$ are set equal to $10^{13}~{\rm s}^{-1}\cdot{\rm site}^{-1}$ for all reactions 61 except the forward reaction of step 7 and the backward reaction of step 8, which both involve a liquid ${\rm H_2O}$ molecule. Values of A for these reactions are set as follows. $A_{\rm fw,7}$ is set equal to $1.43\times10^{10}~{\rm s}^{-1}\cdot{\rm site}^{-1}$, which is the value calculated in our prior work. 45 $F_{\rm act,fw,7}$ and $F_{\rm act,fw,8}$ are set to zero, also following our prior work, 45 since step 7 simply involves forming a hydrogen bond between COH* and a liquid ${\rm H_2O}$ molecule, and step 8 involves proton transfer through a hydrogen bond. 52,53,62 Then, $A_{\rm bw,8}$ is solved for to maintain thermodynamic consistency between steps 6, 7 and 8. Doing this, $A_{\rm bw,8}$ equals 2.25×10^9 s⁻¹·site⁻¹.

Rate constants for adsorption and desorption are simulated using the Hertz-Knudsen (HK) model, ⁴⁹ which computes $A_{\rm fw}$ as the number of collisions per unit time that an ideal gas molecule has with a featureless surface and assumes that $\Delta F_{\rm act,fw} = 0$ and $\Delta F_{\rm act,bw} = -\Delta F_{\rm ads}$

for exergonic adsorption. We have previously shown that such models give adsorption rates for methanol that are several orders of magnitude smaller (depending on the concentration) than the adsorption rate in liquid systems and proposed an alternate method for quantifying the adsorption rate in liquid systems. ⁶³ We found that using this alternate method does not significantly influence the results of this work (see Supporting Information Section 1.8). We hence use the HK model for all adsorption/desorption reactions for simplicity. Additionally, we neglect solvation contributions to $\Delta F_{\rm act,bw}$ for steps 15 and 16. This is done so as not to convolute differences in the simulated CH₃OH dehydrogenation rates between gas and aqueous phases with the free energies of solvation of CO* and H*. Specifically, we find that water solvent destabilizes CO* by 0.14 eV on terrace sites and 0.26 eV on perimeter sites and H* by 0.03 eV on terrace sites and 0.11 eV on perimeter sites (see Table 1). While the destabilization of H* has minimal influence on the simulated rate of methanol dehydrogenation (see Supporting Information Section 1.9), destabilization of CO* increases the rate by up to 3 orders of magnitude (see Supporting Information Section 1.5). FTIR experiments did not consider CO* desorption or conversion by another means, such as WGS⁴¹, so accounting for destabilization in microkinetic modeling would cloud our ability to identify the roles of water solvent observed experimentally.

2.5 Site Balance

Sites are counted as follows. On Pt(111), a site can be considered to be a single Pt atom (or the surface area occupied by a single Pt atom). Analysis of adsorbate geometries (see Supporting Information Figure 10) in perimeter sites indicates that defining a perimeter site is more complicated. This is because some species (e.g., CH₂OH*) bind to both Pt and Al, others (e.g., CH₃OH*, H₂O*) bind to Al and "block" the proximal Pt atom from most – but not all – species, and others (e.g., H*) only bind to Pt and do not block the proximal Al atom at all. This is important, since in the second and third cases, two species could potentially occupy the same "site," depending on how a site is defined. Based on the reaction steps

presented above and the adsorbate geometries presented in Supporting Information Figure 10, this could occur when 1) CH₃OH or H₂O adsorbs to an Al atom simultaneously with H*, and 2) H₂O adsorbs to an Al atom simultaneously with CO*. Accounting for this would require writing a multisite microkinetic model where Pt and Al atoms are counted separately. To our knowledge, this capability does not exist in the MKMCXX code. Hence, we tested the two scenarios as follows. To model scenario 1), we wrote a model where H* does not exist and instead directly desorbs as $\frac{1}{2}$ H₂. For example, instead of CH₃OH*+* \rightleftharpoons CH₂OH*+H*, rxn 3 was written as CH₃OH* \rightleftharpoons CH₂OH*+ $\frac{1}{2}$ H₂. We found this choice has no noticeable impact on the mechanism and impacts the rate by less than an order of magnitude. Further details are provided in Supporting Information Section 1.2. To model scenario 2), we eliminated rxn 2 from the microkinetic model and instead bundled the free energy of H₂O adsorption into step 12. We found that this choice has no noticeable impact on the mechanism or rate. Further details are provided in Supporting Information Sections 1.1. Given the lack of influence of scenarios 1) and 2) on the results, we define one perimeter site as the grouping of Pt atoms plus the proximal Al atom at the Pt/Al₂O₃ perimeter.

2.6 Free Energies

Species free energies (F_i) are set as follows. Free energies of gas phase species (F_i^{gas}) are set equal to the electronic energies calculated using density functional theory (DFT; i.e., the zero point energy and thermal contributions are neglected). These values are for the most part taken from structures calculated in our prior work, ⁴⁴ with some exceptions noted below. Free energies of reaction $(\Delta F_{\text{rxn}}^{\text{gas}})$ and activation in gas phase $(\Delta F_{\text{act,fw}}^{\text{gas}})$ are then calculated as:

$$\Delta F_{\text{rxn or act,fw}}^{\text{gas}} = \left(\sum_{i}^{\text{products or TS}} F_{i}^{\text{gas}}\right) - \left(\sum_{i}^{\text{reactants}} F_{i}^{\text{gas}}\right)$$
(20)

This equation is written using sums since $\Delta F_{\mathrm{rxn}}^{\mathrm{gas}}$ can involve multiple reactant and product

species (e.g., rxn 8 has 2 reactant species and 3 product species); however, we note that $\Delta F_{\rm act,fw}^{\rm gas}$ always involves only 1 TS and 1 reactant species. In general, $\Delta F_{\rm rxn}^{\rm gas}$ and $\Delta F_{\rm act,fw}^{\rm gas}$ used in this work are in good agreement with values calculated previously; ^{34,43} microkinetic modeling results using previously reported values on terrace sites in gas phase are provided in Supporting Information Section 1.1 for comparison. Free energies of reaction and activation in the aqueous (aq) phase are computed by adding the change in the free energy of solvation, $\Delta \Delta F_{\rm rxn}^{\rm solv}$

$$\Delta F_{\rm rxn\ or\ act,fw}^{\rm aq} = \Delta F_{\rm rxn\ or\ act,fw}^{\rm gas} + \Delta \Delta F_{\rm rxn\ or\ act,fw}^{\rm solv}$$
 (21)

where

$$\Delta \Delta F_{\text{rxn or act,fw}}^{\text{solv}} = \left(\sum_{i}^{\text{products or TS}} \Delta F_{i}^{\text{solv}}\right) - \left(\sum_{i}^{\text{reactants}} \Delta F_{i}^{\text{solv}}\right)$$
(22)

and $\Delta F_i^{\rm solv}$ are the calculated free energies of solvation for the different reaction intermediates and TSs. Exceptions are steps 7 and 8; $\Delta F_{\rm act,fw}^{\rm aq}$ for these reactions are estimated as discussed above.

2.7 Solvation Thermodynamics

 $\Delta F_i^{
m solv}$ for reaction intermediates are taken from a previous publication from our group. ⁴⁴ This paper reported values of $\Delta H_i^{
m solv}$ and $T\Delta S_i^{
m solv}$ at 300 K. To scale values of $T\Delta S_i^{
m solv}$ to the reaction temperature used in this work (of 500 K), the values from Ref. ⁴⁴ are multiplied by a factor of 5/3. Solvation thermodynamics for transition states (TSs) are estimated according to a method proposed in our prior publication. ⁴⁴ Briefly, we found that values of $\Delta F_i^{
m solv}$ are linearly correlated to the DFT-calculated partial charges on the oxygen atoms in the alkoxy groups of aldehyde species and the oxygen and hydrogen atoms in the hydroxyl groups of alcohol species. We hence compute the partial charges of TS species using DFT and use them along with the correlation derived in prior work to determine $\Delta F_i^{
m solv}$ for TSs. Further

details are provided in Supporting Information Section 2. Finally, $\Delta F^{\rm solv}$ for a free site * is set to 0 for all reactions.

2.8 Calculation of Structures Not Available in Prior Work

2.8.1 Structural Models

Structures needed to compute $\Delta F_i^{\rm solv}$ for all TSs used in this work as well as $\Delta F_i^{\rm gas}$ for the TSs for steps 3 and 13 on perimeter sites need to be calculated. These structures are calculated using periodic boundary condition DFT calculations using a 4-layer 4 Pt×4 Pt Pt(111) slab as a model for terrace sites and a Pt cluster anchored to an α -Al₂O₃(0001) slab as a model for perimeter sites, following our prior work. ^{39,44,45} Pt(111) slabs are modeled in supercells with lengths of a = b = 11.2 Å and c = 26.8 Å and angles of $\alpha = \beta = 90^{\circ}$ and $\gamma = 120^{\circ}$. Pt/Al₂O₃ perimeter sites are in supercells with lengths of a = b = 10.3 Å and c = 32.7 Å and angles of $\alpha = \beta = 90^{\circ}$ and $\gamma = 55.3^{\circ}$. These models are depicted in Supporting Information Figures S14 and S15.

Pt particles used in our perimeter site models comprise 4 Pt atoms. We have previously shown that $\Delta F_i^{\rm solv}$ is insensitive to the size of the Pt cluster used to model the Pt/Al₂O₃ perimeter site. Specifically, we found the difference in $\Delta F_i^{\rm solv}$ between the Pt₄ cluster and a Pt₄₈ cluster is below 0.10 eV, which is within the standard uncertainty of the modeling method used to compute $\Delta F_i^{\rm solv 44}$. However, the Pt cluster size could influence calculated values of $F_i^{\rm gas}$. Previous literature showed that binding energies and reaction energetics involved in the oxygen reduction reaction calculated using Pt₄ clusters supported on graphene and Al₂O₃ are only minorly different when compared with 6–10 Pt atom clusters. Further, the binding energy of CO* on our Pt₄/Al₂O₃ model is only 0.08 eV more negative than the value calculated by Koleva et al. 66 using a Pt₁₀/ γ -Al₂O₃ model. We find that the binding energy of CO* is 0.24 eV more negative on Pt₄/Al₂O₃ than on Pt(111). Since CO* desorption has the highest DRC (see Table 2), the result of this is that the simulated rate in gas phase is ~2.5 orders of magnitude slower on our perimeter site models than on our

terrace site models. However, this difference does not influence the main conclusion about perimeter sites made in this paper, i.e., that the active sites for aqeuous phase CH_3OH dehydrogenation are on the Pt terraces and that sites at the Pt/Al_2O_3 perimeter are inactive due to H_2O* molecules that bind strongly to Al atoms at the Pt/Al_2O_3 perimeter, hence blocking sites for CH_3OH* . These findings are discussed in detail below.

2.8.2 DFT calculations

DFT calculations are performed using the Vienna Ab initio Simulation Package (VASP) $^{67-69}$ using PAW 2002 pseudopotentials, ^{70,71} the PBE exchange-correlation functional, ^{72,73} and D3 dispersion corrections with Becke-Johnson damping, 74,75 following our prior work. 44 Plane waves are included to an energy cutoff of 400 eV, spin polarization is turned on, and dipole corrections are applied in the direction normal to the surface. Electronic energies are calculated self-consistently and considered to be converged when the difference between subsequent iterations falls below 10^{-6} eV. TS searches are carried out using a combination of the climbing image nudged elastic band (CI-NEB)^{76,77} and dimer methods. ^{78,79} Atoms in the TS structures as well as the top two surface layers are allowed to relax in terrace site calculations, and TS structures and the Pt cluster are allowed to relax in perimeter site calculations. Geometries are considered converged when the magnitudes of the forces on all atoms allowed to relax fall below 0.05 eV/Å. TS structures are verified via their calculated vibrational modes, which are calculated using the center difference method where atoms are displaced by 0.015 Å in the + and - directions in the a, b, and c dimensions. TS searches are performed using Γ-centered Monkhorst–Pack k-point meshes ⁸⁰ of 3×3×1. Partial charges are calculated from these structures using the DDEC6 atomic population analysis method. 81 To compute F_i^{gas} , a single point calculation is performed on the final geometry using a k-point mesh of $7\times7\times1$ to be consistent with energies calculated in our prior work. 34,44

2.9 Rates from experimental data

FTIR data is taken from our previous publication. Experiments were performed on a $Pt/\gamma-Al_2O_3$ catalyst in the presence and absence of H_2O . Experiments done in the absence of H_2O were performed under vacuum at 150°C and 0.5 mbar methanol. Experiments performed in the presence of H_2O exposed the catalyst to 0.5 mbar H_2O prior to exposure to methanol. Both experiments were carried out for up to 30 min and the CO stretching frequency was tracked. The integral of this frequency is proportional to the quantity of methanol consumed. Experimental reaction rates are hence calculated as the rate of change of the CO integral with respect to the reaction time. Rates reported herein are the maximum values for each dataset.

3 Results

3.1 Reaction Energetics

Calculated values of $\Delta F_{\rm rxn}$ and $\Delta F_{\rm act,fw}$ are presented in Table 1. In agreement with prior work, ³⁴ CH₃OH adsorbs more favorably at perimeter sites than terrace sites due to the presence of Lewis acidic Al atoms at the Al₂O₃ interface. ^{82–84} Further, early O–H cleavage is preferred on perimeter sites, whereas early C–H cleavage is preferred on Pt terraces. ^{42,43} CO* binds strongly to both types of sites; however, its binding energy is stronger in perimeter sites than in terrace sites by 0.24 eV. Notably, CH₃OH* and CO* are weakened under solvation in both types of sites, with CH₃OH* destabilized by 0.14 eV in terrace sites and 0.13 eV in perimeter sites, and CO* destabilized by 0.14 eV in terrace sites and 0.26 eV in perimeter sites.

Table 1: Calculated free energies of reaction and activation for possible steps in the methanol dehydrogenation reaction on Pt terrace and Pt/Al_2O_3 perimeter sites in units of eV.

	Type of site	Terrace Sites				Perimeter Sites			
No.	Reaction	$\Delta F_{\rm rxn}^{\rm gas} ({\rm eV})^{\star}$	$F_{\rm act}^{\rm gas}$ (eV)	$\Delta F_{\rm rxn}^{\rm aq} \; ({\rm eV})$	$F_{\rm act}^{\rm aq} \; ({\rm eV})$	$\Delta F_{\rm rxn}^{\rm gas} \; ({\rm eV})^{\star}$	$F_{\rm act}^{\rm gas}$ (eV)	$\Delta F_{\rm rxn}^{\rm aq} \; ({\rm eV})^{\star}$	$F_{\rm act}^{\rm aq} \; ({\rm eV})^{\star\star}$
1	$CH_3OH + * \rightleftharpoons CH_3OH*$	-0.76	NC	−0.62 [*]	NC	-1.15	NC	-1.02	NC
2	$H_2O + * \rightleftharpoons H_2O*$	-0.47	NC	0.77*	NC	-0.95	NC	$-0.92 / -1.16^{\circ}$	NC
3	$CH_3OH* + * \rightleftharpoons CH_2OH* + H*$	-0.48	0.81§	−0.77*	0.79**	-0.61	0.47	-0.43	0.56
4	$CH_2OH* + * \rightleftharpoons CHOH* + H*$	-0.51	0.49	-0.14*	0.73**	0.49	NC	0.47	NC
5	$CHOH* + * \rightleftharpoons COH* + H*$	-0.84	0.51	-1.10*	0.41**	-0.59	NA	-0.17	NA
6	$COH* + * \rightleftharpoons CO* + H*$	-0.38	1.23§	-0.08*	1.39**	-1.21	NA	-1.20	NA
7	$COH* + H_2O \rightleftharpoons COH - H_2O*$	NC	NC	0.28‡	0‡	NA	NA	NA	NA
8	$\mathrm{COH-H_2O*} + * \rightarrow \mathrm{CO*} + \mathrm{H*} + \mathrm{H_2O}$	NC	NC	-0.36‡	0‡	NA	NA	NA	NA
9	$CH_3OH* + * \rightleftharpoons CH_3O* + H*$	0.33	NC	0.44*	NC	-0.51	0.30†	-0.18	0.40
10	$CH_3O* + * \rightleftharpoons CH_2O* + H*$	-0.04	NA	-0.03*	NA	-0.40	1.00†	-0.26	0.92
11	$CH_2O* + * \rightleftharpoons CHO* + H*$	-1.33	NA	−1.42 [*]	NA	-0.45	0.84†	-0.42	0.72
12	$CHO* + * \rightleftharpoons CO* + H*$	-1.17	0.43§	−1.07*	0.43**	-0.56	1.32†	-0.48	1.24
13	$CH_2OH* + * \rightleftharpoons CH_2O* + H*$	0.77	NC	1.18*	NC	-0.31	1.05	-0.01	1.12
14	$CHOH* + * \rightleftharpoons CHO* + H*$	-0.05	0.54	−0.10*	0.45**	-1.25	NA	-1.05	NA
15	$CO* \rightleftharpoons CO + *$	2.19	NC	2.05*,\$	NC	2.43	NC	2.17 [⋄]	NC
16	$H* \rightleftharpoons \frac{1}{2}H_2 + *$	0.68	NC	0.65*,\$	NC	0.64	NC	0.53*	NC

^{*}Taken from Ref. 44

†Taken from Ref. ³⁴

‡Estimated based on values reported in Ref. 45

§Taken from Ref. ⁴³

NC = Not calculated because $\Delta F_{\rm rxn} \geq 0.30$ eV or it is an adsorption/desorption step and $\Delta F_{\rm act}$ is assumed to be 0 or because the reaction is not relevant in this phase.

NA = Not accessible due to a reactant species being unfavorable.

 $^{^{\}star\star} \text{Computed}$ based on a correlation from Ref. 44

[♦] Not used in microkinetic modeling; the gas phase equivalent was used instead.

 $^{^{\}circ} \mathrm{Equivalent}$ value at the clean alumina surface.

The influence of solvation on the calculated reaction energetics is illustrated in Figure 2. This box-and-whisker plot shows the distribution of $\Delta \Delta F^{\rm solv}$ for the reaction and activation free energies in terrace and perimeter sites. The line inside of each box is the median value of $\Delta \Delta F^{\rm solv}$. Most of these are ~ 0 with the exception of $\Delta F^{\rm aq}_{\rm rxn}$ in perimeter sites, which has a median $\Delta \Delta F^{\rm solv}$ of 0.16 eV, indicating that $\Delta F^{\rm aq}_{\rm rxn}$ in perimeter sites tends to be penalized by solvation. We showed in prior work that this is the result of the large entropic penalties that result in forming CH₃O* and CH₂O*, due to the large cavities these adsorbates create in the strongly bound H₂O layer on the Al₂O₃ surface. He range of values in between the tick marks (i.e., the "whiskers") indicates the range of values of $\Delta \Delta F^{\rm solv}$ for each dataset, while the ranges of values spanned by the boxes indicate the interquartile ranges. All datasets have ranges \sim 0.3 eV and interquartile ranges of \sim 0.2 eV except for $\Delta F^{\rm solv}_{\rm rxn}$ in terrace sites, which has a range of nearly 0.7 eV. Specifically, rxns 3-6 have large $\Delta \Delta F^{\rm solv}$ of \sim 0.29 eV, \sim 0.37 eV, \sim 0.26 eV, and \sim 0.30 eV, respectively. These reactions involve CH₂OH* and COH* which have large $\Delta F^{\rm solv}$ due to strong interactions with liquid water 45.

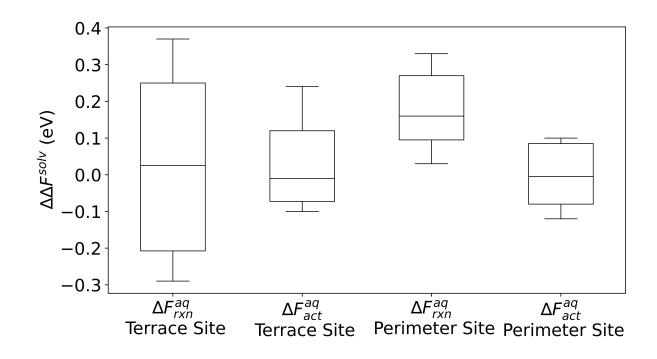


Figure 2: Box-and-whisker plot of the solvation contribution $(\Delta \Delta F^{\text{solv}})$ to free energies of reaction and activation for terrace and perimeter sites. The boxes show the interquartile ranges and the whiskers show the maximum and minimum calculated values. The line inside the box is the median.

3.2 Rates and Mechanisms

Methanol consumption rates are plotted in Figure 3. Specifically, rates simulated in microkinetic modeling are plotted in Figure 3a and rates derived from FTIR data are shown

in Figure 3b. Simulations indicate that in gas phase, the rate on terrace sites is more than 2 orders of magnitude faster than in perimeter sites. In somewhat of a contrast, the experimentally-derived rate on large Pt particles is within the same order of magnitude as that on small Pt particles. This difference could be because simulations are modeling terrace sites or perimeter sites, whereas the Pt particles utilized experimentally comprise both terrace sites and perimeter sites. Alternatively it could be due to the calculated binding energy of CO*, or a combination, or someting else altogether. For this reason, we refrain from making a conclusion about the relative activity of terrace vs perimeter sites in gas phase at this time and instead focus on the influence of solvent.

Both experiments and simulations indicate that water solvent has has a small influence on the rate in terrace sites (which are "modeled" by large Pt particles in experiments). However, simulations and experiments notably disagree on the influence of water on perimeter sites (which are "modeled" by small Pt particles in experiments). Specifically, simulations indicate that solvation slightly increases the rate at perimeter sites (due to slight stabilization of the TS for rxn 12; see below), while experiments indicate that the presence of water decreases the rate on small Pt particles by \sim 1.5 orders of magnitude. This difference suggests a mismatch between experiments and simulations. To understand this more deeply, we investigate the dominant reaction pathways (Figure 4) and rate determining steps (Table 2) for all four models.

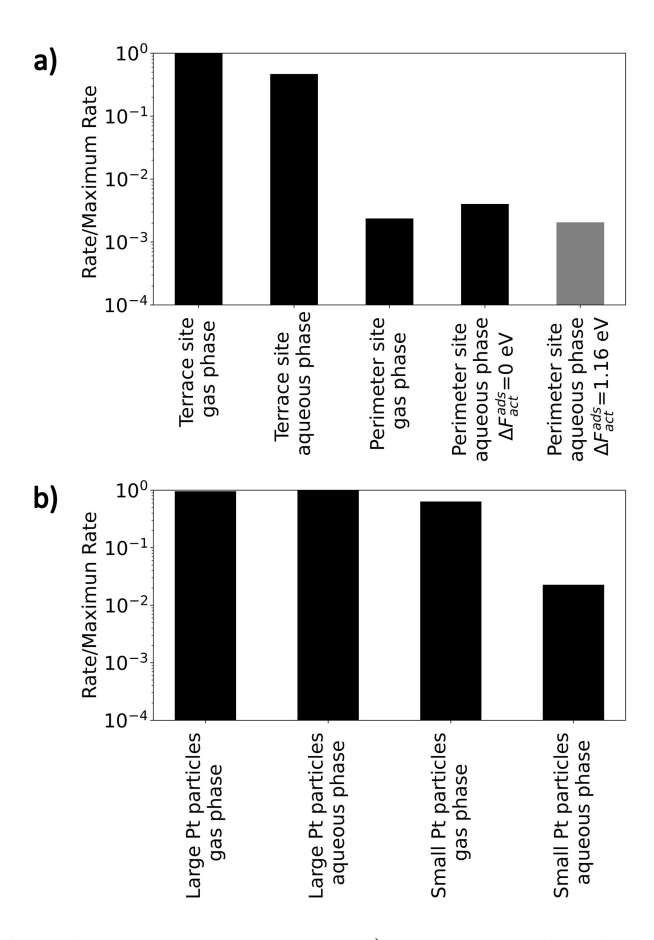


Figure 3: Relative methanol consumption rates. a) Rates simulated in microkinetic modeling relative to the simulated rate on terrace sites in the gas phase. Black bars represent the original model and the gray bar represents a model where methanol adsorption has an activation barrier equal to the desorption free energy of water. b) Rates derived from FTIR data⁴¹ calculated relative to the rate on large Pt particles in the aqueous phase.

Table 2: Steps with degree of rate control value > 0.1 for the different microkinetic models investigated in this work. Values of $\Delta F_{\rm act}^{\rm ads}$ are for CH₃OH adsorption.

Site/phase	Step	calculated DRC value
Terrace/gas	$CO* \rightleftharpoons CO + *$	0.99
Terrace/aqueous	$CO* \rightleftharpoons CO + *$	1.00
Terrace/aqueous	$H* \rightleftharpoons \frac{1}{2}H_2 + *$	0.27
Terrace/aqueous	$CH_3OH* + * \rightleftharpoons CH_2OH* + H*$	-0.27
Perimeter/gas	$CO* \rightleftharpoons CO + *$	0.74
Perimeter/gas	$CHO* + * \rightleftharpoons CO* + H*$	0.43
Perimeter/gas	$H* \rightleftharpoons \frac{1}{2}H_2 + *$	-0.15
Perimeter/aqueous: $\Delta F_{\rm act}^{\rm ads} = 0$	$CO* \rightleftharpoons CO + *$	1.00
Perimeter/aqueous: $\Delta F_{\rm act}^{\rm ads} = 1.16 \text{ eV}$	$CO* \rightleftharpoons CO + *$	0.68
Perimeter/aqueous: $\Delta F_{\rm act}^{\rm ads} = 1.16 \text{ eV}$	$CH_3O* + * \rightleftharpoons CH_2O* + H*$	0.17

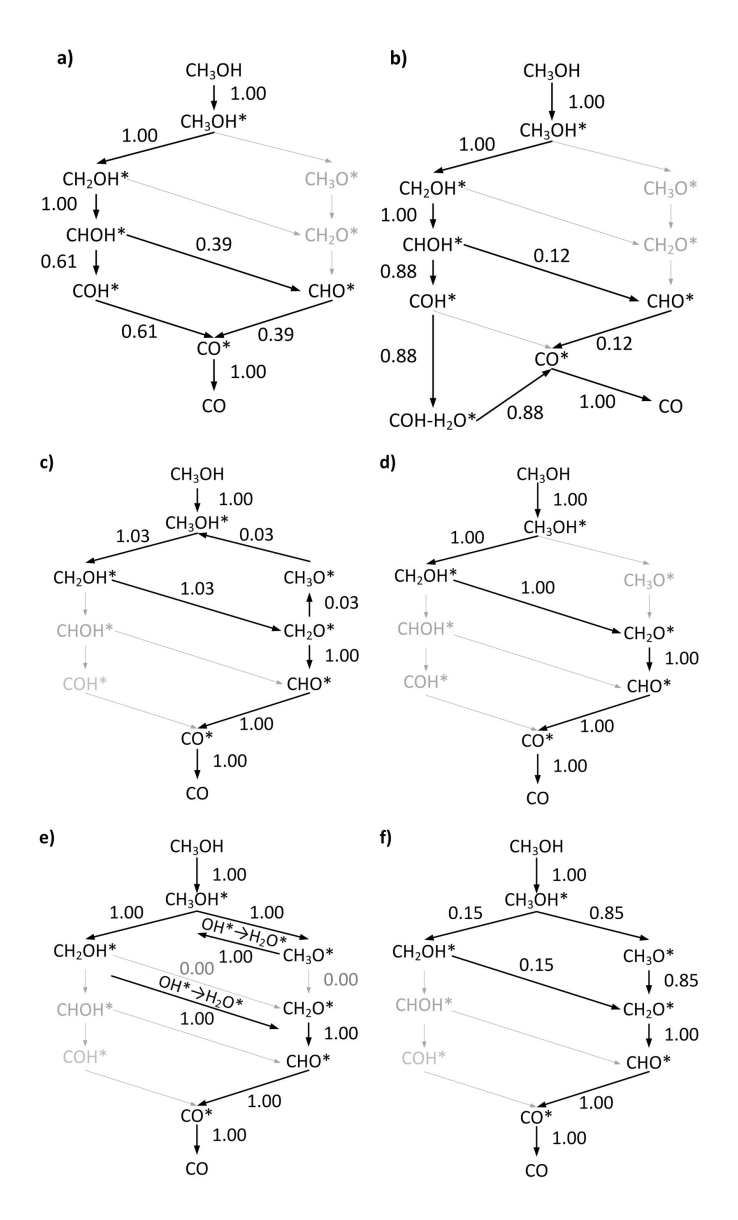


Figure 4: Calculated methanol dehydrogenation reaction mechanisms (black arrows) on a) terrace sites in gas phase, b) terrace sites in aqueous phase, c) perimeter sites in gas phase, d) perimeter sites in aqueous phase (original model), e) perimeter sites in aqueous phase with H₂O* reaction with CH₂O* and CH₃O* steps enabled, f) perimeter sites in aqueous phase where methanol adsorption has an activation barrier equal to the desorption free energy of water. Gray arrows represent thermodynamically and/or kinetically unfavorable reactions. Numbers over each arrow are the reaction rates relative to the rate of methanol adsorption for that model.

3.2.1 Terrace Sites

The dominant reaction pathway on terrace sites in gas phase is presented in Figure 4a. It begins by proceeding through an "alcohol route" where the O-H bond remains intact, in agreement with previous literature. ^{34,42,43} Upon formation of CHOH*, the mechanism branches to CHO*; this is because CHOH* dehydrogenation to COH* has a large activation barrier. However, COH* is thermodynamically preferred over CHO*, so 61% of CHOH* is converted to COH*, while 39% of CHOH* is converted to CHO*. Steps with DRC values greater than 0.1 are presented in Table 2. In terrace sites in gas phase, the only step that fits that criteria is CO* desorption with a DRC value of 0.99.

The mechanism in aqueous phase (Figure 4b) starts out the same as in gas phase but then becomes notably different at the CHOH* branch point. Specifically, the preference to form COH* over CHO* becomes stronger, with 88% of CHOH* going to form COH* and 12% of CHOH* going to form CHO*, due to stabilization of COH* by water. Further, the steady state coverage of COH* is $\sim 55\%$ COH* in the aqueous phase (compared to $\sim 2\%$ in the gas phase; see Supporting Information Section 1.4). Another difference between gas and aqueous phases is that in aqueous phase, COH* dehydrogenation occurs via an H₂O-assisted route involving rxns 7 and 8 due to significantly more facile kinetics. Further, desorption of both CO* and $\mathrm{H_{2}}*$ have DRCs greater than 0.1 in aqueous phase (Table 2), with values of 1.00 and 0.27, respectively. Further, CH₃OH* dehydrogenation to CH₂OH* has a DRC value of -0.27 in aqueous phase. This is due to stabilization of both CH_2OH* and COH*by water. Specifically, stabilization of CH₂OH* via rxn 3 and subsequent stabilization of COH* via rxn 5 results in the larger preference for COH* over CHO* at the branch point. However, weakening of CO* via rxn 6 results in slower CO* formation kinetics (and hence slower CH₃OH consumption kinetics). If rxn 3 were slower, the proportion of CHO* to COH* would be larger and hence formation of CO* would be less impacted by water. Similarly, if H₂* desorption were faster, formation of CO* via rxn 6 would be faster. A more detailed explanation is provided in Supporting Information Section 1.6.

3.2.2 Perimeter Sites

The dominant reaction pathway on perimeter sites in the gas phase is presented in Figure 4c. We find that early C-H cleavage is preferred, similar to the mechanism on terrace sites. However, CH_2OH* is then entirely converted to CH_2O* . Once CH_2O* is formed, a small amount is converted to CH_3O* ; however, the majority is converted to CHO*. Perimeter sites hence follow an "aldehyde" pathway following formation of CH_2OH* . A similar mechanism was found for CH_3OH dehydrogenation on Pt/CeO_2 . Surface coverage in this model is $\sim 60\%$ CO* and $\sim 40\%$ CHO*. The reactions with DRC values greater than 0.1 are CO* desorption and CHO* dehydrogenation to CO*, with DRC values of 0.74 and 0.43, due to the strong binding energy of CO* and large activation energy of CHO* dehydrogenation, respectively (see Table 1). Further, H_2* desorption has a DRC value of -0.15; if this reaction were slower, the coverage of CO* would increase relative to CHO*.

The mechanism for perimeter sites in the aqueous phase (Figure 4d) is largely the same as in gas phase, with the only minor differences being that CH₂O* dehydrogenation does not run in reverse and that CO* desorption is the only step with a DRC value greater than 0.1 (equal to 1.00 in this case), due to a 0.08 eV reduction in the barrier for CHO* dehydrogenation. As a result, the rate in the aqueous phase is slightly larger than in gas phase. This observation is in contrast to experiments performed on small Pt particles, which showed a reduction in the rate in the presence of water (see Figure 3b).

3.2.3 Possible Explanations for Differences Between Experiments and Theory

The difference in the presence of water on small Pt particles observed experimentally vs. Pt_4/Al_2O_3 perimeter site models used in simulations suggests a "mismatch" between experiments and theory. One possibility for this could be that H_2O* molecules adsorbed at Pt/Al_2O_3 perimeter sites are protonating aldehyde intermediates (e.g., $CH_2O* + H_2O* \rightleftharpoons CH_2OH* + OH*)$, hence pushing the reaction backward (towards hydrogenation) and hindering the rate of methanol dehydrogenation. To investigate this possibility, we compute

the free energies of such steps; they are presented in Supporting Information Section 1.3. We find that reaction of H_2O* with CH_3O* to form CH_3OH* and CH_2O* to form CH_2OH* have free energies more negative than 0.3 eV (which is our tolerance for inclusion in microkinetic modeling). We hence enable these steps in microkinetic modeling, assuming the activation barriers for these steps are equal to 0, using reasoning developed in our prior work that proton transfer through a hydrogen bond has an activation barrier $\sim 0.45,52,53,62$ Details of these simulations are presented in Supporting Information Section 1.3, and the resulting mechanism is presented in Figure 4e. We find that H_2O* indeed participates in the mechanism by reacting with CH_3O* to form CH_3OH* ; the OH* that is formed then reacts with CH_2OH* to form CH_2O* . Beyond that, the mechanism is the same as in our original model. Further, the rate is unaffected (see Supporting Information Section 1.3), suggesting that H_2O* reaction with CH_xO* species at the Pt/Al_2O_3 perimeter is not responsible for the decrease in rate on small Pt particles observed experimentally.

A second possibility, which was proposed in our prior publication, 41 is that diffusion of CH₃OH* across the Al₂O₃ interface is hindered by the strongly bound H₂O* adlayer 86,87 and that this affects the rate on small particles. To test this scenario, we compute the barrier of CH₃OH* diffusion across an Al₂O₃ slab in vacuum versus in the presence of a H₂O* adlayer. Details of these calculations are provided in Supporting Information Section 1.7. Briefly, to simulate the aqueous phase scenario, a H₂O* adlayer is built around the TS identified in the gas phase and then the TS structure is re-relaxed. Doing this, we find that the barrier for CH₃OH* diffusion decreases, i.e., the H₂O* adlayer stabilizes the TS for CH₃OH* diffusion on Al₂O₃.

A failing with that model is that it does not account for the requirement that CH_3OH* must displace adsorbed H_2O* molecules while diffusing across the Al_2O_3 surface. To test this scenario, we increase $\Delta F_{\rm act,fw}^{\rm aq}$ for CH_3OH adsorption (step 1) from 0 to 1.16 eV, which is the free energy of desorption of a H_2O* molecule from $\alpha-Al_2O_3$ in aqueous phase (note that the free energy of H_2O* desorption from pristine $\alpha-Al_2O_3$ and Pt_4/Al_2O_3 are modestly different;

this is due to steric hindrance on the supported Pt models). This is akin to modeling the barrier to $\mathrm{CH_3OH*}$ adsorbing to a perimeter site as the free energy required to displace a $\mathrm{H_2O*}$ molecule on the $\mathrm{Al_2O_3}$ surface. Doing this, we find a $\sim 50\%$ reduction in the rate of methanol consumption. This rate is compared with the other simulated rates in Figure 3a (gray bar). The mechanism is shown in Figure 4f. It is largely similar to the original scenario (i.e., where the activation barrier for $\mathrm{CH_3OH}$ adsorption was set to 0) except that a branch point occurs at $\mathrm{CH_3OH*}$, with 15% of $\mathrm{CH_3OH*}$ being converted to $\mathrm{CH_2OH*}$ and 85% being converted to $\mathrm{CH_3O*}$. While this scenario gives behavior that is more in line with observations from FTIR, the slight decrease in rate observed in microkinetic modeling is noticeably less dramatic than the multiple order of magnitude decrease observed experimentally. We discuss reasons for this in the next section.

4 Discussion

While the rate of methanol dehydrogenation on Pt/Al_2O_3 perimeter sites has only minor dependence on the activation barrier for methanol adsorption, the steady state *coverages* (Supporting Information Figure 4) are strongly dependent on this quantity. Specifically, using the activated adsorption model, the coverage of H_2O* at the Pt/Al_2O_3 perimeter is $\sim 50\%$ (with the remaining $\sim 50\%$ being occupied by CO*), while using the unactivated model, the H_2O* coverage is ~ 0 , while the CO* coverage is $\sim 100\%$.

The larger coverage of H_2O* suggests that reactions involving H_2O* should have more appreciable rates. We hence enabled the steps involving reaction of H_2O* with CH_3O* to form CH_3OH* and CH_2O* to form CH_2OH* along with activated methanol adsorption in our microkinetic modeling simultaneously. Doing this, the methanol consumption rate on Pt/Al_2O_3 perimeter sites decreased to ~ 0 . This decrease is more dramatic than observed in FTIR; however, we propose it is the combination of these two things that causes the decrease in rate observed experimentally. Specifically, we propose that strongly bound H_2O*

molecules both inhibit CH₃OH binding at the Pt/Al₂O₃ perimeter and promote hydrogenation of CH₃OH fragments that are bound there. In fact, our microkinetic models suggest the combination of these two effects completely shuts the reaction down at the Pt/Al₂O₃ perimeter, hence suggesting that activity observed experimentally on small Pt particles is due to the Pt terraces that exist in the system. This is a difference between the simulated and experimental systems: the models of perimeter sites used in simulations only comprise perimeter sites, whereas the small Pt particles used in experiments mainly but not entirely comprise perimeter sites. Hence, the experimentally observed decrease in activity going from 4.6 nm to 1.0 nm particles is \sim 1.5 orders of magnitude, whereas going from terrace site to perimeter site models results in a complete loss of activity.

Taken together, these results suggest that small Pt particles are less active than large Pt particles due to strongly bound H_2O* molecules at the Pt/Al_2O_3 perimeter that block sites for methanol dehydrogenation. The active sites for aqueous phase CH_3OH dehydrogenation on Pt/Al_2O_3 catalysts are hence Pt terrace sites, regardless of particle size; the mechanism is that presented in Figure 4b, and the steps with significant DRC values are CO* desorption (positive DRC \sim 1), H_2* desorption (positive DRC <1), and CH_3OH* dehydrogenation to CH_2OH* (negative DRC > -1).

5 Conclusion

In this work, we combined multiscale modeling with microkinetic modeling and Fourier transform infrared spectroscopy to determine the mechanism for methanol dehydrogenation on supported Pt/Al_2O_3 catalysts under aqueous phase. A goal of this work was to determine if the active sites are Pt terrace or Pt/Al_2O_3 perimeter sites. Our findings indicate that sites at the Pt/Al_2O_3 perimeter are inactive due to the presence of strongly bound H_2O* molecules, which inhibit adsorption of CH_3OH and also push the reaction in the reverse by donating protons to CH_xO* species. The active sites are hence the Pt terrace sites.

Water has little influence on the rate of CH_3OH dehydrogenation in terrace sites, but it has a significant impact on the mechanism. Specifically, water stabilizes CH_2OH* and COH*, which pushes the mechanism through a $COH-H_2O*$ intermediate. This intermediate alters the equilibrium between COH* and CO*. Steps with significant degrees of rate control are CO* desorption, H_2* desorption, and CH_3OH* dehydrogenation to CH_2OH* . Some ways to improve the rate of methanol dehydrogenation on Pt/Al_2O_3 catalysts are to destabilize CO* and (to a lesser extent) H* as well as to decrease (make more positive) the free energies of solvation of CH_2OH* and COH*.

6 Acknowledgments

This research was funded by the National Science Foundation under award numbers CHE-1764296 and CHE-1764304. Simulations were performed on the Ohio Supercomputer Center and the Palmetto Supercomputing Cluster, which is maintained by the Cyberinfrastructure Technology Integration Group at Clemson University.

References

- (1) Pérez, R. S.; Souza, M. M. V. M.; Tapanes, N. C. O.; Diaz, G. C.; Aranda, D. A. G. Production of Hydrogen from Aqueous Phase Reforming of Glycerol: Economic Evaluation. *Engineering* **2014**, *6*, 12–18.
- (2) Pipitone, G.; Zoppi, G.; Pirone, R.; Bensaid, S. A critical review on catalyst design for aqueous phase reforming. *International Journal of Hydrogen Energy* **2022**, *47*, 151–180.
- (3) Okolie, J. A.; Patra, B. R.; Mukherjee, A.; Nanda, S.; Dalai, A. K.; Kozinski, J. A. Futuristic applications of hydrogen in energy, biorefining, aerospace, pharmaceuticals and metallurgy. *International Journal of Hydrogen Energy* 2021, 46, 8885–8905.

- (4) Sutton, A. D.; Waldie, F. D.; Wu, R.; Schlaf, M.; 'Pete'Silks, L. A.; Gordon, J. C. The hydrodeoxygenation of bioderived furans into alkanes. *Nature Chemistry* 2013 5:5 2013, 5, 428–432.
- (5) He, Z.; Cui, M.; Qian, Q.; Zhang, J.; Liu, H.; Han, B. Synthesis of liquid fuel via direct hydrogenation of CO2. *Proceedings of the National Academy of Sciences* **2019**, *116*, 12654–12659, doi: 10.1073/pnas.1821231116.
- (6) Sarma, S. J.; Pachapur, V.; Brar, S. K.; Bihan, Y. L.; Buelna, G. Hydrogen biorefinery: Potential utilization of the liquid waste from fermentative hydrogen production. Renewable and Sustainable Energy Reviews 2015, 50, 942–951.
- (7) Godina, L. I.; Tokarev, A. V.; Simakova, I. L.; Mäki-Arvela, P.; Kortesmäki, E.; Gläsel, J.; Kronberg, L.; Etzold, B.; Murzin, D. Y. Aqueous-phase reforming of alcohols with three carbon atoms on carbon-supported Pt. *Catalysis Today* **2018**, *301*, 78–89.
- (8) Kim, T. W.; Kim, H. D.; Jeong, K. E.; Chae, H. J.; Jeong, S. Y.; Lee, C. H.; Kim, C. U. Catalytic production of hydrogen through aqueous-phase reforming over platinum/ordered mesoporous carbon catalysts. *Green Chemistry* **2011**, *13*, 1718–1728.
- (9) Rahman, M. M. Aqueous-Phase Reforming of Glycerol over Carbon-Nanotube-Supported Catalysts. *Catalysis Letters* **2020**, *150*, 2674–2687.
- (10) Coronado, I.; Stekrova, M.; Reinikainen, M.; Simell, P.; Lefferts, L.; Lehtonen, J. A review of catalytic aqueous-phase reforming of oxygenated hydrocarbons derived from biorefinery water fractions. *International Journal of Hydrogen Energy* 2016, 41, 11003–11032.
- (11) Grabow, L. C.; Gokhale, A. A.; Evans, S. T.; Dumesic, J. A.; Mavrikakis, M. Mechanism of the Water Gas Shift Reaction on Pt: First Principles, Experiments, and

- Microkinetic Modeling. The Journal of Physical Chemistry C 2008, 112, 4608–4617, doi: 10.1021/jp7099702.
- (12) Li, D.; Li, Y.; Liu, X.; Guo, Y.; Pao, C.-W.; Chen, J.-L.; Hu, Y.; Wang, Y. NiAl2O4 Spinel Supported Pt Catalyst: High Performance and Origin in Aqueous-Phase Reforming of Methanol. *ACS Catalysis* **2019**, *9*, 9671–9682, doi: 10.1021/acscatal.9b02243.
- (13) Davda, R. R.; Shabaker, J. W.; Huber, G. W.; Cortright, R. D.; Dumesic, J. A. A review of catalytic issues and process conditions for renewable hydrogen and alkanes by aqueous-phase reforming of oxygenated hydrocarbons over supported metal catalysts. Applied Catalysis B: Environmental 2005, 56, 171–186.
- (14) Tokarev, A. V.; Kirilin, A. V.; Murzina, E. V.; Eränen, K.; Kustov, L. M.; Murzin, D. Y.; Mikkola, J. P. The role of bio-ethanol in aqueous phase reforming to sustainable hydrogen. *International Journal of Hydrogen Energy* 2010, 35, 12642– 12649.
- (15) Luo, N.; Fu, X.; Cao, F.; Xiao, T.; Edwards, P. P. Glycerol aqueous phase reforming for hydrogen generation over Pt catalyst – Effect of catalyst composition and reaction conditions. Fuel 2008, 87, 3483–3489.
- (16) Tao, J.; Hou, L.; Yan, B.; Chen, G.; Li, W.; Chen, H.; Cheng, Z.; Lin, F. Hydrogen Production via Aqueous-Phase Reforming of Ethylene Glycol over a Nickel-Iron Alloy Catalyst: Effect of Cobalt Addition. *Energy & Fuels* **2020**, *34*, 1153–1161, doi: 10.1021/acs.energyfuels.9b02149.
- (17) Godina, L. I.; Kirilin, A. V.; Tokarev, A. V.; Murzin, D. Y. Aqueous Phase Reforming of Industrially Relevant Sugar Alcohols with Different Chiralities. ACS Catalysis 2015, 5, 2989–3005.
- (18) Godina, L. I.; Heeres, H.; Garcia, S.; Bennett, S.; Poulston, S.; Murzin, D. Y. Hy-

- drogen production from sucrose via aqueous-phase reforming. *International Journal of Hydrogen Energy* **2019**, *44*, 14605–14623.
- (19) Pipitone, G.; Zoppi, G.; Frattini, A.; Bocchini, S.; Pirone, R.; Bensaid, S. Aqueous phase reforming of sugar-based biorefinery streams: from the simplicity of model compounds to the complexity of real feeds. *Catalysis Today* **2020**, *345*, 267–279.
- (20) Hare, B. J.; Carcamo, R. A. G.; Daemen, L. L.; Cheng, Y.; Getman, R. B.; Sievers, C. Poisoning of Pt/γ-Al2O3 Aqueous Phase Reforming Catalysts by Ketone and Diketone-Derived Surface Species. ACS Catalysis 2024, 14, 1480–1493.
- (21) Gu, G. H.; Wittreich, G. R.; Vlachos, D. G. Microkinetic modeling of aqueous phase biomass conversion: Application to ethylene glycol reforming. *Chemical Engineering* Science 2019, 197, 415–418.
- (22) Wu, R.; Wang, L. Insight into the solvent effects on ethanol oxidation on Ir(100).

 Physical Chemistry Chemical Physics 2023, 25, 2190–2202.
- (23) Li, G.; Wang, B.; Resasco, D. E. Solvent effects on catalytic reactions and related phenomena at liquid-solid interfaces. *Surface Science Reports* **2021**, *76*, 100541.
- (24) Li, G.; Komarneni, M. R.; Wang, B.; Marinkovic, N.; Resasco, D. E. Cooperative roles of water and metal-support interfaces in the selective hydrogenation of cinnamaldehyde over cobalt boride catalysts. *Cell Reports Physical Science* **2023**, *4*, 101367.
- (25) Ruiz-Lopez, M. F.; Francisco, J. S.; Martins-Costa, M. T. C.; Anglada, J. M. Molecular reactions at aqueous interfaces. *Nature Reviews Chemistry* **2020**, *4*, 459–475.
- (26) Lustemberg, P. G.; Palomino, R. M.; Gutiérrez, R. A.; Grinter, D. C.; Vorokhta, M.; Liu, Z.; Ramírez, P. J.; Matolín, V.; Ganduglia-Pirovano, M. V.; Senanayake, S. D.; Rodriguez, J. A. Direct Conversion of Methane to Methanol on Ni-Ceria Surfaces:

- Metal-Support Interactions and Water-Enabled Catalytic Conversion by Site Blocking. Journal of the American Chemical Society 2018, 140, 7681–7687.
- (27) Stanciakova, K.; Weckhuysen, B. M. Water–active site interactions in zeolites and their relevance in catalysis. *Trends in Chemistry* **2021**, *3*, 456–468.
- (28) Zhao, S. et al. Remarkable active-site dependent H2O promoting effect in CO oxidation.

 Nature Communications 2019 10:1 2019, 10, 1–9.
- (29) Merte, L. R.; Peng, G.; Bechstein, R.; Rieboldt, F.; Farberow, C. A.; Grabow, L. C.; Kudernatsch, W.; Wendt, S.; Lægsgaard, E.; Mavrikakis, M.; Besenbacher, F. Watermediated proton hopping on an iron oxide surface. *Science* **2012**, *336*, 889–893.
- (30) Zaki, M. I.; Hasan, M. A.; Al-Sagheer, F. A.; Pasupulety, L. Surface chemistry of acetone on metal oxides: IR observation of acetone adsorption and consequent surface reactions on silica-alumina versus silica and alumina. *Langmuir* 2000, 16, 430–436.
- (31) Lehnert, K.; Claus, P. Influence of Pt particle size and support type on the aqueousphase reforming of glycerol. *Catalysis Communications* **2008**, *9*, 2543–2546.
- (32) Jenness, G. R.; Christiansen, M. A.; Caratzoulas, S.; Vlachos, D. G.; Gorte, R. J. Site-Dependent Lewis Acidity of γAl_2O_3 and Its Impact on Ethanol Dehydration and Etherification. The Journal of Physical Chemistry C **2014**, 118, 12899–12907.
- (33) Copeland, J. R.; Shi, X. R.; Sholl, D. S.; Sievers, C. Surface interactions of C2 and C3 polyols with γAl_2O_3 and the role of coadsorbed water. *Langmuir* **2013**, 29, 581–593.
- (34) Xie, T.; Hare, B. J.; Meza-Morales, P. J.; Sievers, C.; Getman, R. B. Identification of the Active Sites in the Dehydrogenation of Methanol on Pt/Al2O3 Catalysts. The Journal of Physical Chemistry C 2020, 124, 19015–19023.
- (35) Ciftci, A.; Peng, B.; Jentys, A.; Lercher, J. A.; Hensen, E. J. M. Support effects in

- the aqueous phase reforming of glycerol over supported platinum catalysts. *Applied Catalysis A: General* **2012**, *431-432*, 113–119.
- (36) Lu, H.; Zhong, Y.; Jie, Y.; Yin, P.; Zhao, X. J.; Feng, Y. L.; Shen, T. Y.; Guo, J. Y.; Zhang, W.; Pu, M.; Yan, H. A DFT study on methanol decomposition over single atom Pt/CeO2 catalysts: the effect of the position of Pt. Physical Chemistry Chemical Physics 2023, 25, 14232–14244.
- (37) Walker, E. A.; Mitchell, D.; Terejanu, G. A.; Heyden, A. Identifying Active Sites of the Water–Gas Shift Reaction over Titania Supported Platinum Catalysts under Uncertainty. ACS Catalysis 2018, 8, 3990–3998.
- (38) Iwasita, T. Electrocatalysis of methanol oxidation. *Electrochimica Acta* **2002**, *47*, 3663–3674.
- (39) Alias, M. S.; Kamarudin, S. K.; Zainoodin, A. M.; Masdar, M. S. Active direct methanol fuel cell: An overview. *International Journal of Hydrogen Energy* 2020, 45, 19620– 19641.
- (40) Wu, J.; Huang, Y.; Ye, W.; Li, Y.; Wu, J.; Huang, Y.; Ye, W.; Li, Y. CO2 Reduction: From the Electrochemical to Photochemical Approach. Advanced Science 2017, 4, 1700194.
- (41) Hare, B. J.; Carcamo, R. A. G.; Xie, T.; Meza-Morales, P. J.; Getman, R. B.; Sievers, C. Active sites and effects of co-adsorbed H_2O on isolated methanol dehydrogenation over $Pt/\gamma Al_2O_3$. Journal of Catalysis **2021**, 402, 218–228.
- (42) Desai, S. K.; Neurock, M.; Kourtakis, K. A Periodic Density Functional Theory Study of the Dehydrogenation of Methanol over Pt(111). *The Journal of Physical Chemistry B* **2002**, *106*, 2559–2568.

- (43) García-Muelas, R.; Li, Q.; López, N. Density functional theory comparison of methanol decomposition and reverse reactions on metal surfaces. ACS Catalysis 2015, 5, 1027– 1036.
- (44) Carcamo, R. A. G.; Zhang, X.; Estejab, A.; Zhou, J.; Hare, B. J.; Sievers, C.; Sarupria, S.; Getman, R. B. Differences in solvation thermodynamics of oxygenates at Pt/Al2O3 perimeter versus Pt(111) terrace sites. *iScience* **2023**, *26*, 105980.
- (45) Bodenschatz, C. J.; Xie, T.; Zhang, X.; Getman, R. B. Insights into how the aqueous environment influences the kinetics and mechanisms of heterogeneously-catalyzed COH* and CH3OH* dehydrogenation reactions on Pt(111). Physical Chemistry Chemical Physics 2019, 21, 9895–9904.
- (46) Zhang, X.; Defever, R. S.; Sarupria, S.; Getman, R. B. Free Energies of Catalytic Species Adsorbed to Pt(111) Surfaces under Liquid Solvent Calculated Using Classical and Quantum Approaches. *Journal of Chemical Information and Modeling* 2019, 59, 2190–2198.
- (47) Filot, I. A. W.; van Santen, R. A.; Hensen, E. J. M. The Optimally Performing Fischer-Tropsch Catalyst. Angewandte Chemie International Edition 2014, 53, 12746–12750, https://doi.org/10.1002/anie.201406521.
- (48) Filot, I. A. W.; Broos, R. J. P.; Rijn, J. P. M. V.; Heugten, G. J. H. A. V.; Santen, R. A. V.; Hensen, E. J. M. First-Principles-Based Microkinetics Simulations of Synthesis Gas Conversion on a Stepped Rhodium Surface. ACS Catalysis 2015, 5, 5453–5467.
- (49) Filot, I. Introduction to microkinetic modeling, i ed.; Technische Universiteit Eindhoven, 2018.
- (50) Campbell, C. T. The Degree of Rate Control: A Powerful Tool for Catalysis Research.

 ACS Catalysis 2017, 7, 2770–2779.

- (51) Kandoi, S.; Greeley, J.; Sanchez-Castillo, M. A.; Evans, S. T.; Gokhale, A. A.; Dumesic, J. A.; Mavrikakis, M. Prediction of experimental methanol decomposition rates on platinum from first principles. *Topics in Catalysis* **2006**, *37*, 17–27.
- (52) Nie, X.; Luo, W.; Janik, M. J.; Asthagiri, A. Reaction mechanisms of CO2 electrochemical reduction on Cu(1 1 1) determined with density functional theory. *Journal of Catalysis* **2014**, *312*, 108–122.
- (53) Janik, M. J.; Taylor, C. D.; Neurock, M. First-Principles Analysis of the Initial Electroreduction Steps of Oxygen over Pt(111). *Journal of The Electrochemical Society* **2009**, *156*, B126.
- (54) Zheng, M.; Zhou, X.; Zhou, Y.; Li, M. Theoretical insights into mechanisms of electrochemical reduction of CO2 to ethylene catalyzed by Pd3Au. *Applied Surface Science* **2022**, *572*, 151474.
- (55) Ranea, V. A.; Schneider, W. F.; Carmichael, I. DFT characterization of coverage dependent molecular water adsorption modes on α - Al_2O_3 (0001). Surface Science 2008, 602, 268–275.
- (56) Phatak, A. A.; Koryabkina, N.; Rai, S.; Ratts, J. L.; Ruettinger, W.; Farrauto, R. J.; Blau, G. E.; Delgass, W. N.; Ribeiro, F. H. Kinetics of the water–gas shift reaction on Pt catalysts supported on alumina and ceria. *Catalysis Today* 2007, 123, 224–234.
- (57) Lee, W. T.; Thomas, F.; Masel, R. L. Methanol oxidation on (2×1)Pt(110): does the C-O or O-H bond break first? Surface Science 1998, 418, 479-483.
- (58) Greeley, J.; Mavrikakis, M. Competitive Paths for Methanol Decomposition on Pt(111).

 Journal of the American Chemical Society 2004, 126, 3910–3919.
- (59) Flaherty, D. W.; Yu, W. Y.; Pozun, Z. D.; Henkelman, G.; Mullins, C. B. Mechanism

- for the water–gas shift reaction on monofunctional platinum and cause of catalyst deactivation. *Journal of Catalysis* **2011**, *282*, 278–288.
- (60) Kung, K. Y.; Chen, P.; Wei, F.; Shen, Y. R.; Somorjai, G. A. Sum-frequency generation spectroscopic study of CO adsorption and dissociation on Pt(111) at high pressure and temperature. *Surface Science* **2000**, *463*, L627–L633.
- (61) Sholl, D. S.; Steckel, J. A. In *Density functional theory a practical introduction*; Steckel, J. A., Ed.; Wiley, 2009.
- (62) Árnadóttir, L.; Stuve, E. M.; Jónsson, H. The effect of coadsorbed water on the stability, configuration and interconversion of formyl (HCO) and hydroxymethylidyne (COH) on platinum (1 1 1). *Chemical Physics Letters* **2012**, *541*, 32–38.
- (63) Zhang, X.; Savara, A.; Getman, R. B. A Method for Obtaining Liquid-Solid Adsorption Rates from Molecular Dynamics Simulations: Applied to Methanol on Pt(111) in H2O. Journal of Chemical Theory and Computation 2020, 16, 2680–2691.
- (64) Nigam, S.; Majumder, C. ORR viability of alumina-supported platinum nanocluster: exploring oxidation behaviour by DFT. Physical Chemistry Chemical Physics 2017, 19, 19308–19315.
- (65) Zandkarimi, B.; Alexandrova, A. N. Dynamics of Subnanometer Pt Clusters Can Break the Scaling Relationships in Catalysis. *Journal of Physical Chemistry Letters* 2019, 10, 460–467.
- (66) Koleva, I. Z.; Aleksandrov, H. A.; Vayssilov, G. N. Influence of the adsorption of CO on the electronic structure of platinum clusters and nanowires deposited on CeO2(111) and γ-Al2O3(001) surfaces. Catalysis Today 2020, 357, 442–452.
- (67) Kresse, G.; Hafner, J. Ab initio molecular dynamics for liquid metals. *Physical Review B* **1993**, 47, 558–561.

- (68) Kresse, G.; Furthmüller, J. Efficiency of ab-initio total energy calculations for metals and semiconductors using a plane-wave basis set. *Computational Materials Science* 1996, 6, 15–50.
- (69) Kresse, G.; Furthmüller, J. Efficient iterative schemes for ab initio total-energy calculations using a plane-wave basis set. *Physical Review B* **1996**, *54*, 11169–11186.
- (70) Mortensen, J. J.; Hansen, L. B.; Jacobsen, K. W. Real-space grid implementation of the projector augmented wave method. *Physical Review B - Condensed Matter and Materials Physics* 2005, 71, 35109.
- (71) Kresse, G.; Joubert, D. From ultrasoft pseudopotentials to the projector augmentedwave method. *Physical Review B* **1999**, *59*, 1758.
- (72) Perdew, J. P.; Burke, K.; Ernzerhof, M. Generalized Gradient Approximation Made Simple. *Physical Review Letters* **1996**, *77*, 3865–3868.
- (73) Perdew, J. P.; Burke, K.; Ernzerhof, M. Generalized Gradient Approximation Made Simple [Phys. Rev. Lett. 77, 3865 (1996)]. *Physical Review Letters* **1997**, 78, 1396.
- (74) Grimme, S.; Antony, J.; Ehrlich, S.; Krieg, H. A consistent and accurate ab initio parametrization of density functional dispersion correction (DFT-D) for the 94 elements H-Pu. *The Journal of Chemical Physics* **2010**, *132*, 154104.
- (75) Grimme, S.; Ehrlich, S.; Goerigk, L. Effect of the damping function in dispersion corrected density functional theory. *Journal of Computational Chemistry* **2011**, *32*, 1456–1465.
- (76) Henkelman, G.; Uberuaga, B. P.; Jónsson, H. A climbing image nudged elastic band method for finding saddle points and minimum energy paths. The Journal of Chemical Physics 2000, 113, 9901.

- (77) Henkelman, G.; Jónsson, H. Improved tangent estimate in the nudged elastic band method for finding minimum energy paths and saddle points. *The Journal of Chemical Physics* **2000**, *113*, 9978.
- (78) Henkelman, G.; Jónsson, H. A dimer method for finding saddle points on high dimensional potential surfaces using only first derivatives. *The Journal of Chemical Physics* **1999**, *111*, 7010.
- (79) Heyden, A.; Bell, A. T.; Keil, F. J. Efficient methods for finding transition states in chemical reactions: Comparison of improved dimer method and partitioned rational function optimization method. *The Journal of Chemical Physics* **2005**, *123*, 224101.
- (80) Monkhorst, H. J.; Pack, J. D. Special points for Brillouin-zone integrations. *Physical Review B* **1976**, *13*, 5188–5192.
- (81) Limas, N. G.; Manz, T. A. Introducing DDEC6 atomic population analysis: part 4. Efficient parallel computation of net atomic charges, atomic spin moments, bond orders, and more. RSC Advances 2018, 8, 2678–2707.
- (82) Boon, J.; van Kampen, J.; Hoogendoorn, R.; Tanase, S.; van Berkel, F. P. F.; van Sint Annaland, M. Reversible deactivation of γ-alumina by steam in the gas-phase dehydration of methanol to dimethyl ether. Catalysis Communications 2019, 119, 22–27.
- (83) Hare, B. J.; Carcamo, R. A. G.; Getman, R. B.; Sievers, C. Surface Chemistry of Ketones and Diketones on Lewis Acidic γ – Al₂O₃ Probed by Infrared Spectroscopy. Journal of Physical Chemistry C 2022, 126, 17554–17568.
- (84) Wang, R.; Zhao, Z.; Gao, P.; Chen, K.; Gan, Z.; Fu, Q.; Hou, G. Impact of Adsorption Configurations on Alcohol Dehydration over Alumina Catalysts. *The Journal of Physical Chemistry C* **2022**, *126*, 10073–10080.

- (85) Ngouana-Wakou, B. F.; Cornette, P.; Valero, M. C.; Costa, D.; Raybaud, P. An Atomistic Description of the γ-Alumina/Water Interface Revealed by Ab Initio Molecular Dynamics. Journal of Physical Chemistry C 2017, 121, 10351–10363.
- (86) Argyris, D.; Ho, T.; Cole, D. R.; Striolo, A. Molecular dynamics studies of interfacial water at the alumina surface. *Journal of Physical Chemistry C* **2011**, *115*, 2038–2046.
- (87) Petrik, N. G.; Huestis, P. L.; LaVerne, J. A.; Aleksandrov, A. B.; Orlando, T. M.; Kimmel, G. A. Molecular Water Adsorption and Reactions on α – Al₂O₃(0001) and α-Alumina Particles. The Journal of Physical Chemistry C 2018, 122, 9540–9551.